Acta Crystallographica Section B
Structural Science
ISSN 0108-7681

Incommensurate structure of $Ca_2Al_2O_5$ at high temperatures – structure investigation and Raman spectroscopy

Biljana Lazic,* Hannes Krüger, Volker Kahlenberg, Jürgen Konzett and Reinhard Kaindl

Institute of Mineralogy and Petrography, University of Innsbruck, Innrain 52, 6020 Innsbruck, Austria

Correspondence e-mail: biljana.lazic@uibk.ac.at

Received 14 February 2008
Accepted 27 May 2008

A high-temperature X-ray diffraction study revealed that brownmillerite-type $Ca_2Al_2O_5$ transforms to an incommensurately modulated structure at elevated temperatures. Single crystals of $Ca_2Al_2O_5$ were synthesized in an end-loaded piston cylinder press at 2.5 GPa and 1273 K. The diffraction pattern observed at 1090 (10) K by *in situ* single-crystal diffraction experiments can be indexed by an *I*-centred orthorhombic cell and a modulation wavevector of $\mathbf{q} = 0.595\,(1)\mathbf{c}^*$. A (3 + 1)-dimensional model in superspace group $Imma(00\gamma)s00$ was used to refine the modulated structure. The structure is assembled from two building units: (i) layers of corner-sharing $[AlO_6]$ octahedra, stacked along **b** alternate with (ii) layers of *zweier* single chains of $[AlO_4]$ tetrahedra running along **a**. The modulated structure arises from an aperiodic sequence of two different configurations of the chains within the tetrahedral layers. The modulated high-temperature phase of $Ca_2Al_2O_5$ is isotypic to the modulated high-temperature modification of $Ca_2Fe_2O_5$. A large hysteresis was found in the phase-transition temperature. On heating, the transition occurs at *ca* 1075 (10) K; on cooling, satellite reflections can be observed down to 975 (10) K. The characterization of $Ca_2Al_2O_5$ is completed by Raman spectroscopy, including a partial interpretation of the spectra.

1. Introduction

Brownmillerites, as one of the most stable oxygen-deficient materials related to perovskites, have many technological applications. A survey of patent databases revealed 56 US patents, as well as 40 European patents using the term 'brownmillerite'. Amongst others, they include uses for solid fuel cells, dense membranes for the partial oxidation of hydrocarbons, and separation of oxygen from gas streams. Recent investigations have found large magnetoresistance effects in Mn-based brownmillerite-type materials (Battle *et al.*, 2002).

Brownmillerite-type compounds of the general composition $A_2B_2O_5$ (A^{2+}; B^{3+}) consist of two main building units: layers of perovskite-type corner-sharing $[BO_6]$ octahedra and *zweier* single chains of $[BO_4]$ tetrahedra. The alternate stacking of perovskite-like layers and sheets of tetrahedral chains results in a three-dimensional network with the *A* ions in interstitial voids. These structures can be considered as defect perovskites, with *ca* 17% of vacancies on the anion positions (Kahlenberg & Shaw, 2001). The oxygen vacancies are distributed in the chains along the [110] directions of the primitive cubic perovskite cell resulting in alternating layers of tetrahedrally and octahedrally coordinated trivalent cations

(Hadermann *et al.*, 2007; Abakumov *et al.*, 2005). More complex brownmillerites ($A_2BB'O_5$) show two different types of *B* cations, which may occupy the tetrahedrally or the octahedrally coordinated site, respectively. Disorder of the *B* and *B*′ cations on tetrahedral and octahedral positions is frequently observed.

So far, brownmillerite-type materials with the following cations have been reported: *A* = (Ca, Sr, Ba, La) and *B* = (Al, Cr, Mn, Fe, Co, Cu, Ga, In). However, in the strict sense the name brownmillerite corresponds to a calcium aluminoferrite with the composition Ca_2FeAlO_5 (Hansen *et al.*, 1928; Colville & Geller, 1971). Owing to the fact that Ca_2FeAlO_5 is an important phase in Portland cement clinkers, a considerable amount of research was carried out on this compound and the corresponding chemical systems. According to Taylor (1997), the solid solution series $Ca_2(Fe_{1-x}Al_x)_2O_5$ exists from $x = 0$ to $x = 0.7$ at ambient pressures. The iron-rich compositions up to $x = 0.235$ adopt the space group *Pnma*, whereas the samples with high Al concentration crystallize in the space group *I*2*mb* (Fukuda & Ando, 2002). The Al-rich end-member $Ca_2Al_2O_5$ can only be prepared at high pressures and temperatures (*e.g.* 2.5 GPa, 1273 K), but can be quenched to room conditions (Kahlenberg & Shaw, 2001; Kahlenberg *et al.*, 2000; Aggarwal *et al.*, 1972).

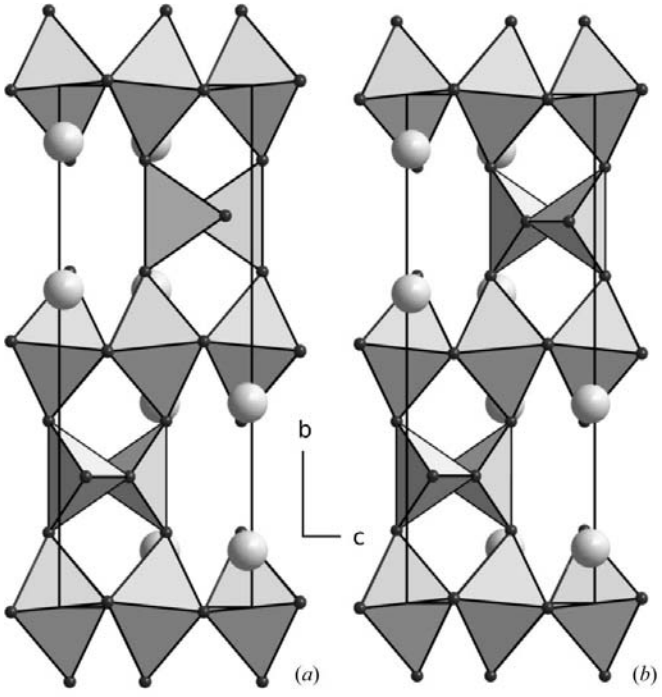

Figure 1
Most brownmillerite-type structures crystallize in space groups *Pnma* or *I*2*mb*: (*a*) *Pnma* symmetry with alternating layers of L and R tetrahedral *zweier* chains; (*b*) space group *I*2*mb*, with only one type of tetrahedral chain.

The main structural differences between the *Pnma* and *I*2*mb* symmetries can be identified in the tetrahedral layers. The tetrahedral chains can adopt two mirror-related configurations, which are denoted as left-handed (L) and right-handed (R; Milat *et al.*, 1993). *Pnma* brownmillerites show layers of R chains, alternating with layers of L chains (Fig. 1*a*). Non-centrosymmetric structures of *I*2*mb* symmetry exhibit only one type (R or L) of chain in the structure, depending on the absolute configuration (Fig. 1*b*). A third space group is frequently reported: *Imma*, which requires disorder of R and L chains in all tetrahedral layers. It can be assumed that some of the *Imma* structures are approximations of more complex superstructures, as shown in the following examples. Greaves *et al.* (1975) suggested that a more complex ordering of the tetrahedral layers/chains may be present in the *Imma* structure of $Sr_2Fe_2O_5$. A superstructure based on alternating R and L chains within the tetrahedral layer was observed by Abakumov *et al.* (2001) by electron diffraction on Sr_2MnGaO_5. A (3 + 1)-dimensional superspace model was employed by Lambert *et al.* (2002) to describe the commensurate superstructures of $Ca_2Co_{2-x}Al_xO_5$. A similar approach was applied to Sr_2MnGaO_5 (Abakumov *et al.*, 2003). $Ca_2Fe_2O_5$, which was investigated with high-temperature neutron powder diffraction by Berastegui *et al.* (1999), has been reported to transform to the *Imma* structure at *ca* 973 K. Fukuda & Ando (2002) and Redhammer *et al.* (2004) have previously mentioned possible modulations in the high-temperature phase of $Ca_2Fe_2O_5$ because of weak unexplained peaks in the powder XRD patterns. A more recent high-temperature single-crystal X-ray investigation showed that each tetrahedral layer indeed exhibits the same number of L and R chains; they are not, however, randomly distributed but are incommensurately ordered, as shown in Fig. 2 (Krüger & Kahlenberg, 2005). The present study reports an isostructural modulated high-temperature phase of the aluminium end-

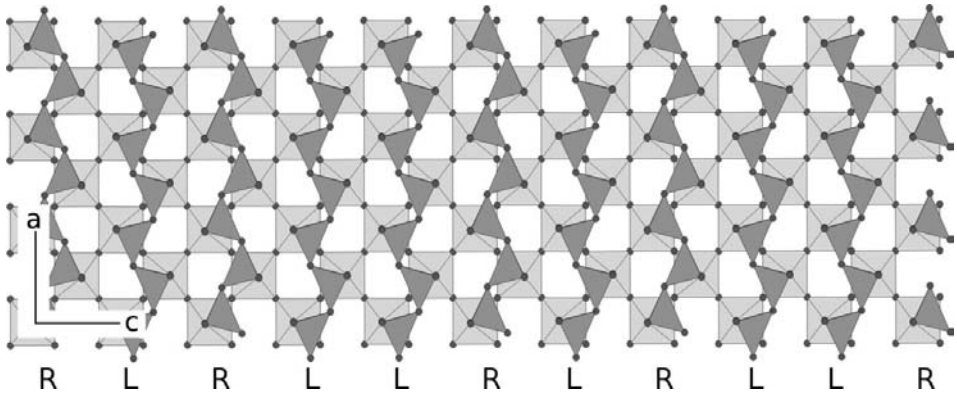

Figure 2
Example of an aperiodic sequence of R and L tetrahedral chains as in the incommensurate high-temperature structures of $Ca_2Al_2O_5$ and $Ca_2Fe_2O_5$. The figure presents an octahedral layer (bright) and a layer of tetrahedral chains (dark). The wavevector of the modulation is oriented horizontally.

Table 1
Experimental details.

Crystal data	
Chemical formula	$Ca_2Al_2O_5$
M_r	214.12
Cell setting, superspace group	Orthorhombic, *Imma*(00γ)*s*00 (No. 74.2)
Temperature (K)	1090 (10)
a, b, c (Å)	5.2699 (5), 14.6984 (15), 5.4196 (5)
V (Å^3)	419.80 (7)
Modulation wavevector	$\mathbf{q}$ = 0.595 (1)$\mathbf{c}^*$
Z	4
D_x (Mg m^{-3})	3.388
Radiation type	Mo $K\alpha$
μ (mm^{-1})	3.04
Crystal form, colour	Fragment, colourless
Crystal size (mm)	0.14 × 0.12 × 0.1
Data collection	
Diffractometer	Stoe IPDS 2
Data collection method	Rotation method
No. of frames measured	120
Range in ω; increment (°)	0–180; 1.5
Exposure time per frame (min)	20
Absorption correction	Integration
T_{min}	0.794
T_{max}	0.834
No. of measured reflections (main, sat)	1871, 3680
No. of observed reflections (main, sat)	1646, 1731
Criterion for observed reflections	$I > 3\sigma(I)$
R_{int}	0.053
θ_{max} (°)	29.1
Refinement	
Refinement on	F
R (all, main, sat)	0.069, 0.039, 0.154
wR (all, main, sat)	0.068, 0.057, 0.102
S	3.52
No. of reflections (main, sat)	319, 529
No. of parameters	43
H-atom treatment	No H atoms present
Weighting scheme	Based on measured s.u.'s; $w = 1/[\sigma^2(F) + 0.0001F^2]$
$(\Delta/\sigma)_{max}$	< 0.0001
$\Delta\rho_{max}$, $\Delta\rho_{min}$ (e Å^{-3})	1.16, −1.04

Computer programs used: *X-AREA*, *X-RED* (Stoe & Cie, 2005), *JANA*2000 (Petříček *et al.*, 2000).

member of the brownmillerite solid-solution series $Ca_2(Fe_{1-x}Al_x)_2O_5$.

2. Experimental

2.1. Sample preparation and high-pressure synthesis

The starting material for the high-pressure, high-temperature synthesis was a ceramic precursor prepared from a stoichiometric mixture of dried $CaCO_3$ (Merck 98%) and α-Al_2O_3 (Fluka 98%) in a molar ratio of 2:1. A total of 1.5 g of the educts was homogenized in an agate mortar, pressed into pellets and heated in air to 1523 K. The material was sintered twice for 24 h with intermediate grinding, before it was finally quenched to ambient conditions. Powder X-ray diffraction showed the presence of a mixture of two phases: $Ca_3Al_2O_6$ (ICDD entry 38-1429) and $Ca_{12}Al_{14}O_{33}$ (ICDD entry 09-413). The precursor material (0.03 g) was pulverized and filled into an Au capsule. The capsule was sealed and placed in an NaCl-pyrophyllite-BN assembly. For the subsequent HP/HT synthesis experiment a Boyd and England-type piston cylinder with a half-inch pressure vessel was employed (Mirwald *et al.*, 1975). The experiment was performed at a pressure of 2.5 GPa and temperatures of 1273 K for 72 h. Pressure was calibrated against the albite → jadeite + quartz and quartz → coesite transitions. The temperature was measured using a Ni–Cr–Ni (*K*-type) thermocouple. Temperature and pressure were controlled by a computer during the entire run duration. After the HP/HT treatment, the sample was isobarically quenched by turning off the power of the furnace (the sample cooled down to ambient temperature within a few minutes) and then rapidly decompressed.

2.2. X-ray diffraction

A prismatic transparent crystal with good optical quality was selected for the single-crystal data collection, which was performed on a Stoe IPDS-II diffractometer. The results of the diffraction experiment confirmed that single crystals of $Ca_2Al_2O_5$ (Kahlenberg *et al.*, 2000) had been obtained. For the high-temperature investigation the crystal was fixed in a 0.1 mm (outer diameter) fused quartz capillary. A *Heatstream* device (as provided by Stoe) was used for the high-temperature single-crystal diffraction experiment. The *Heatstream* furnace (mounted underneath the sample on the omega axis) supplied a vertical flow of hot nitrogen gas to heat the sample. The stability of the temperature was achieved using a constant flow of N_2 and a stabilized power unit. Data for the modulated phase were collected at 1090 (10) K, and subsequently corrected for absorption using a model of the crystal shape based on indexed faces. Corrections for Lorentz, polarization and air-absorption effects were applied. Further details on the data collection are summarized in Table 1.[1]

Owing to the very limited amount of sample material obtained from the HT/HP synthesis (*ca* 0.03 g), a thermal analysis investigation such as DTA could not be applied to determine the character of the transition and to determine the transition temperature. Instead, a series of 28 single-crystal diffraction experiments covering a temperature range from 930 to 1085 K were performed. Each experiment covered the same range of 20° in ω (1.5° per frame). Long exposure times (30 min per frame) were chosen, to account for the weak intensities of the satellite reflections. After changing the temperature between the data collections, the system was allowed to equilibrate for *ca* 30–40 min. The first experiment was performed at *ca* 1070 K, followed by 14 measurements down to 930 K. Subsequently, another 14 data collections were carried out raising the temperature to 1085 K. The data reduction of all 28 measurements was carried out using the same scaling factor and the same peak profiles to achieve comparability between the experiments. The evolution of the

[1] Supplementary data for this paper are available from the IUCr electronic archives (Reference: SN5068). Services for accessing these data are described at the back of the journal.

intensities of the five most intense satellite reflections as a function of temperature is shown in Fig. 3.

2.3. Raman spectroscopy

Samples were excited by the 514.5 nm emission line of an Ar^+ laser through a 50× long-working distance objective (numerical aperture 0.5). The size and power of the laser spot on the sample surface was approximately 3 µm (diameter) and 5 mW, respectively. The spectral resolution, experimentally determined by measuring the full width at half maximum of the Rayleigh line, was *ca* 1.8 cm^{-1}. The dispersed light was collected by a 1024 × 256 open-electrode CCD detector. A confocal pinhole was set to 1000 µm; spectra were recorded unpolarized. All spectra were baseline-corrected assuming linear background and deconvoluted Voigt functions using the built-in spectrometer software *Labspec*4 (Horiba Jobin Yvon, 2004). Raman shifts were calibrated by regular adjusting of the zero-order position of the grating and the Rayleigh line of a (100) polished single-crystal silicon wafer. The accuracy of the determined band positions should be better than 0.5 cm^{-1}.

The *in situ* high-temperature Raman experiments were performed in a Linkam THMS 1500 heating–freezing stage with a quartz window and a ceramic crucible, mounted to a Labram HR-800 Raman micro-spectrometer by Horiba Jobin Yvon. Measurements were performed between 373 and 1073 K in steps of 100 K. Temperature precision and accuracy, checked by measuring the thermal shift of the TO–LO phonon of a (100) polished single-crystal silicon wafer, was around ± 5 K.

3. Crystal structure

A first diffraction experiment at ambient temperature revealed that the diffraction pattern of $Ca_2Al_2O_5$ could be indexed with the orthorhombic *I*-centred unit cell that has been reported by Kahlenberg *et al.* (2000). After heating to 1090 K this orthorhombic cell was essentially retained. The thermal expansion of the unit-cell volume is *ca* 3%. However, a more detailed analysis of the diffraction data based on precession-type oriented sections of the reciprocal space revealed the presence of satellite reflections (Fig. 4), which were not observed in the room-temperature experiment. Thus, it can be concluded that a phase transition had occurred. The incommensurate satellite reflections can be indexed using a **q** vector of $(0,0,\gamma)$ (de Wolff, 1974) assigning them to the next main reflection along **c***, which is not absent due to the *I* centring. The value of γ has been determined and refined to 0.595 (1) using the *X-Area* software (Stoe & Cie, 2005).

The extinction symbol of the main reflections *I*–(*ab*) conforms to the space groups *Im*2*a* (No. 46) and *Imma* (No. 74). Furthermore, a special reflection condition for the satellites is evident: 0*klm* reflections with $m \neq 2n$ are not observed. Since only first-order satellite reflections were detected, no satellite reflections could be seen in the 0*kl* layer. In summary, the diffraction pattern is consistent with the (3 + 1)-dimensional superspace group *Imma*$(00\gamma)s00$ (No. 74.2; Janssen *et al.*, 2004). Consequently, the model of the (3 + 1)-dimensional high-temperature structure of $Ca_2Fe_2O_5$ (Krüger & Kahlenberg, 2005) was employed as a starting point for the crystal structure refinements. Full-matrix least-squares refinements were carried out using the software *JANA*2000 (Petříček *et al.*, 2000). The calculations proved the hypothesis that the high-temperature structures of the iron ($Ca_2Fe_2O_5$) and the aluminium end-member ($Ca_2Al_2O_5$) are isotypic. The ordering of L and R tetrahedral chains was modelled with crenel

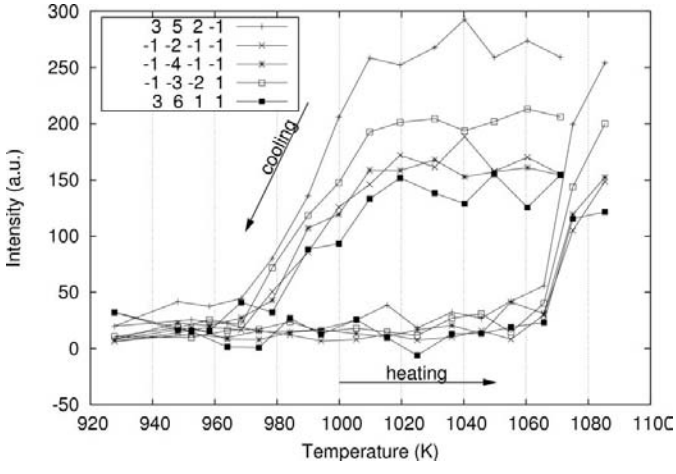

Figure 3
*I*2*mb*–*Imma*$(00\gamma)s00$ phase transition of $Ca_2Al_2O_5$ observed by intensity changes of five strong satellite reflections. There were 28 consecutive single-crystal diffraction experiments performed during one cooling–heating cycle, starting at 1070 K. A large hysteresis in the transition temperature is evident.

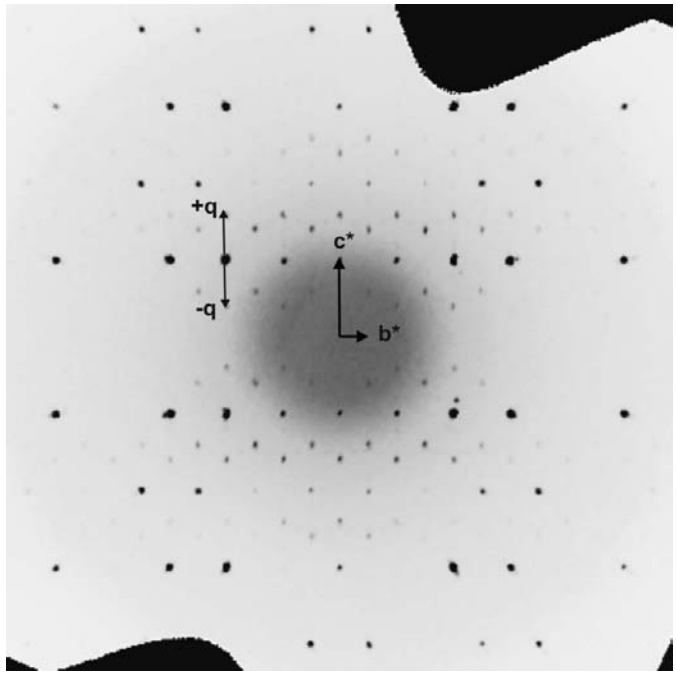

Figure 4
Reciprocal space section (1*kl*) reconstructed from the imaging plate data. First-order satellite reflections can be seen and the corresponding **q** vector is shown.

Table 2
Fourier coefficients of the modulation functions: $u_i(x_4) = A_{1,i} \sin(2\pi x_4) + B_{1,i} \cos(2\pi x_4)$, $i = 1, 2, 3$, and x_4^0 centres of crenel occupation functions of the width $\Delta = 0.5$.

Atom	x_4^0	$A_{1,1}$	$A_{1,2}$	$A_{1,3}$	$B_{1,1}$	$B_{1,2}$	$B_{1,3}$
Al1	–	−0.0017 (3)	0	0	0	0	0
Al2	0.1471 (13)	–	–	–	–	–	–
Ca1	–	−0.0049 (2)	0	0	0.0064 (2)	0	0
O1	–	−0.0012 (6)	0	−0.0004 (7)	0	0.0009 (2)	0
O2	–	0.0036 (8)	0	0	0.0117 (7)	0	0
O3	0.6844 (13)	–	–	–	–	–	–

Table 3
Interatomic distances including averages (ave) and extrema caused by the modulation.

Atoms	d_{ave} (Å)	d_{min} (Å)	d_{max} (Å)	Symmetry codes
Al1—O1	1.8942 (19)	1.8889 (12)	1.9006 (13)	$-1+x, y, z$
	1.895 (2)	1.8888 (12)	1.9006 (12)	$1-x, -y, 1-z$
	1.8952 (19)	1.8889 (12)	1.9006 (13)	$1-x, y, z$
	1.894 (2)	1.8888 (12)	1.9006 (12)	$-1+x, -y, 1-z$
Al1—O2	2.124 (3)	2.124 (3)	2.125 (3)	x, y, z
				$-x, -y, 1-z$
Al2—O2	1.743 (3)	1.739 (3)	1.748 (3)	$1+x, y, z$
				$1+x, \frac{1}{2}-y, z$
Al2—O3	1.787 (4)			$\frac{3}{2}-x, \frac{1}{2}-y, \frac{3}{2}-z$
	1.801 (4)			$1-x, y, z$
Ca1—O1	2.458 (3)	2.437 (2)	2.477 (2)	$-1+x, y, -1+z$
	2.456 (3)	2.437 (2)	2.477 (2)	$1-x, y, -1+z$
	2.501 (3)	2.484 (3)	2.515 (3)	$-1+x, -y, 1-z$
	2.498 (3)	2.484 (3)	2.515 (3)	$1-x, -y, 1-z$
Ca1—O2	2.351 (3)	2.351 (3)	2.352 (3)	x, y, z
	2.697 (4)	2.585 (4)	2.794 (4)	$-\frac{1}{2}-x, 1+y, \frac{1}{2}-z$
	2.682 (4)	2.585 (4)	2.794 (4)	$\frac{1}{2}-x, 1+y, \frac{1}{2}-z$
Ca1—O3	2.3440 (19)	2.3389 (19)	2.3481 (19)	$\frac{1}{2}-x, \frac{1}{2}-y, \frac{1}{2}-z$
	2.3442 (19)	2.3389 (19)	2.3481 (19)	$-\frac{1}{2}+x, \frac{1}{2}-y, \frac{1}{2}-z$

occupation modulation functions for the tetrahedrally coordinated aluminium (Al2), as well as for the O atom interconnecting the tetrahedra (O3). A detailed description and reasons for this approach have been described by Lambert *et al.* (2002) and Krüger & Kahlenberg (2005). The final R factors and further details of the refinement calculations are given in Table 1. If compared with the data published by Krüger & Kahlenberg (2005) it can be noticed that the R factors for the modulated structure are larger, whereas other parameters are comparable. This can be attributed to the quality of the data. Even with much longer exposure times (20 min), the average intensities of the satellite reflections are rather weak. The average $I/\sigma(I)$ of the satellites was 4.3, with 43% being above the observability limit [$I > 3\sigma(I)$], whereas the satellite intensities used by Krüger & Kahlenberg (2005) had an $I/\sigma(I)$ ratio of 7.0 and 54% were observed. The refined superspace model of the structure, as defined by fractional atomic coordinates, anisotropic displacement parameters and Fourier coefficients of the modulation functions are given in Table 2 and the supplementary data. Selected atomic distances are listed in Table 3. A table of the bonding angles can be found in the supplementary material. Figures have been prepared using the computer programs *DIAMOND* (Brandenburg & Berndt, 2001) and *ATOMS* (Dowty, 2000).

Table 4
Bond-valence sums (BVS), including averages (ave) and extrema caused by the modulation.

Atom	BVS_{ave}	BVS_{min}	BVS_{max}
Al1	2.416 (6)	2.416 (6)	2.416 (5)
Al2	2.683 (12)	2.665 (12)	2.698 (12)
Ca1	2.011 (5)	2.009 (5)	2.013 (5)
O1	1.957 (5)	1.943 (4)	1.974 (4)
O2	1.615 (6)	1.612 (6)	1.619 (7)
O3	1.971 (10)	1.963 (10)	1.982 (10)

The temperature of the phase transition from the *I2mb* structure to the modulated phase was determined by temperature-dependent monitoring of five selected satellite reflections (Fig. 3). Their intensities stay almost constant upon cooling from 1070 to 1010 K. Further cooling decreases their intensities until they disappear below 970 K. After increasing the temperature again, the satellites start to reappear at 1065 K and come back to their original intensity values at 1085 K. Thus, the phase transition shows a large hysteresis of almost 100 K. The rate of the intensity changes with the temperature of the satellite reflections, $\Delta I/\Delta T$, is significantly different for the transition during heating and cooling. At the transition from the modulated to the low-temperature phase, satellite intensities decrease over a range of 40 K. Their increase during the transition from the low-temperature to the high-temperature phase takes place over a 20 K range. No diffuse scattering could be observed within the whole temperature range of the transition.

4. Discussion

Atomic distances and angles have been calculated as a function of the internal coordinate t, distortion parameters for the octahedrally and the tetrahedrally coordinated aluminium atom were derived for ten separate t sections. Table 3 lists the maximum (max), minimum (min) and average (av) values observed in the t range from 0 to 1. Bond-valence sums (Brown & Altermatt, 1985) were calculated and are listed in Table 4. The underbonded character of the Al atoms has already been discussed by Kahlenberg & Shaw (2001). The low bond-valence sum of the O atom connecting the tetrahedra and the octahedra is already evident in the structural model of Kahlenberg *et al.* (2000). As expected, at high temperatures the bond-valence sums are even lower.

The relative thermal expansion of $Ca_2Al_2O_5$ from ambient conditions to 1090 K is anisotropic, with the largest component of 1.6% along **b**, 0.9% along **a** and 0.5% in the direction of **c**. Similar relations have been observed in $Ca_2Fe_2O_5$. The pronounced expansion along **b** can be explained by the fact that the bonds of the tetrahedrally coordinated Al atoms are stronger than the bonds in the octahedral arrangement. Since

the layers are oriented perpendicular to **b**, the thermal expansion is dominated by the octahedral layers along the **b** direction. This can also be shown by calculating the relative dilatation of the O2—O2 distance across the octahedra, as well as that of the O2—O2 distance across the tetrahedra: from ambient conditions to 1090 K, the octahedral layers expand by 2.1%, whereas the tetrahedral layers expand by only 0.9 %. The O2—Al2—O2 angle increases from 125.3° at room temperature to 128.6° (128.1–129.7°) in the modulated structure, indicating that the tetrahedra become more stretched along **b** in the high-temperature phase.

The O3—Al2—O3 angles change from 107.2° at room temperature to 108.2° at high temperature, thus becoming closer to the ideal value of 109.4° (Kahlenberg *et al.*, 2000). Altogether the distortion of the tetrahedra increase with temperature, as quantitatively expressed by the quadratic elongation (q.e.) and the angle variance (a.v.), as defined by Robinson *et al.* (1971). Concerning the tetrahedra at ambient temperatures, significant distortions have been reported (q.e. = 1.014; a.v. = 62.3), although the modulated high-temperature phase exhibits even more pronounced distortions (q.e. = 1.020–1.023; a.v. = 85.2–98.9). These values are even higher than those observed in the modulated high-temperature structure of $Ca_2Fe_2O_5$ (Krüger & Kahlenberg, 2005), where tetrahedral distortions of up to 1.016 (a.v.) and 70.1 (q.e.) can be found. A reverse trend can be observed for the distortions of the Al1 coordination octahedra [1.008/8.5 at room temperature and 1.007/2.6–4.7 at high temperature (a.v./q.e)]. The same trend can be observed for the octahedrally coordinated iron in $Ca_2Fe_2O_5$.

In addition to analysing the coordination polyhedra themselves, their linkage has been studied. The angle Al2—O3—Al2 gives information on the degree of chain stretching. The temperature dependence of this angle (129.5° at room temperature, 130.1° at 1090 K) shows that there is no pronounced change in the chain stretching.

The arrangement of the octahedra in the perovskite-type layers deviates from the ideal perovskite aristotype. Within the equatorial plane the rotation around the [100] axis is *ca* 5.4° at room temperature and varies between 5.2 and 6.2° in the modulated structure.

Comparing the *I*2*mb*–*Imma*(00γ)*s*00 transition of $Ca_2Al_2O_5$ to the *Pnma*–*Imma*(00γ)*s*00 transition of $Ca_2Fe_2O_5$, one difference can be noted: in the high-temperature single-crystal XRD experiments on $Ca_2Fe_2O_5$ (Krüger *et al.*, 2006) no pronounced hysteresis was observed. The same study reports that the *Pnma*–*Imma*(00γ)*s*00 transition of $Ca_2Fe_2O_5$ shows a temperature interval where the two phases coexist. Since the phase transition of $Ca_2Al_2O_5$ lacks a change in lattice-centring, a phase coexistence cannot be directly observed by diffraction methods. However, the slow change in satellite intensities (1010–970 K, Fig. 3) can be considered as an indication for phase coexistence. A continuous change in the volume fraction of the modulated structure could be an explanation for the change of satellite intensities. Owing to the nature of the modulated structure a change in the amplitude of the modulation can be excluded. However, to prove the postulated phase-coexistence, high-temperature, high-resolution transmission electron microscopy would be the method of choice.

As driving forces for the phase transitions in brownmillerites, dipole–dipole interactions have been discussed (Abakumov *et al.*, 2005; Krüger & Kahlenberg, 2005). As electric dipoles are associated with the tetrahedral chains (Milat *et al.*, 1993; Krekels *et al.*, 1993) the energetically favoured arrangement of the tetrahedral layer would show alternating R and L chains. Such an alternation sequence induces a higher distortion of the octahedral layers, as shown by Abakumov *et al.* (2005). The equilibrium of these competing forces (dipole interactions/chain ordering *versus* distortion in the octahedral layers) could change with temperature or chemical composition [as in $Ca_2MnGa_{1-x}Al_xO_5$ (Abakumov *et al.*, 2005)] and cause the transition to a different ordering of the chains. Potential reasons have been identified in the anisotropic displacement behaviour: the thermal expansion of $Ca_2Al_2O_5$ along the **c** direction is smaller than along the other axes. Therefore, the distance between neighbouring chains increases less than the distance between the tetrahedral layers. Furthermore, the expansion of the octahedra (along **b**) is larger than the expansion of other structural units.

4.1. Raman spectroscopy

To the best of our knowledge the Raman spectrum of the unmodulated room-temperature structure of polycrystalline $Ca_2Al_2O_5$ is unknown and is, therefore, described in detail. Several high-temperature Raman experiments at increasing temperatures up to 1073 K were also carried out and the results will be discussed. $Ca_2Al_2O_5$ crystallizes in the space group *I*2*mb*, point/factor group C_{2v}. Simple factor group analysis by the software packages *Vibratz* (Dowty, 2006) and *SAM* (symmetry-adapted modes; Kroumova *et al.*, 2003) yielded 53 theoretical possible vibrational modes

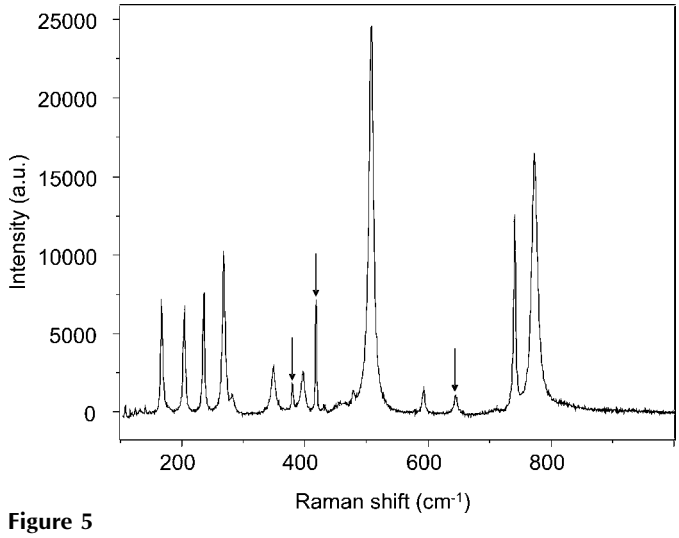

Figure 5
Raman spectrum of $Ca_2Al_2O_5$ at ambient temperature. The three bands marked with arrows result from the underlying sample holder.

Table 5
Raman shifts (shift), relative intensities (rel. int.), full width at half-maximum (FWHM) and temperature dependence ($\Delta\nu/\Delta T$) of experimentally determined bands in the spectra of $Ca_2Al_2O_5$ at 296, 373 and 1073 K.

Relative intensities are integrated band areas relative to the most intense bands (506, 505 and 493 cm^{-1})

$Ca_2Al_2O_5$ 296 K			$Ca_2Al_2O_5$ 373 K			$Ca_2Al_2O_5$ 1073 K				
Shift	Rel. int.	FWHM	Shift	Rel. int.	FWHM	Shift	Rel. int	FWHM	Assignment	$\Delta\nu/\Delta T$ (cm^{-1} K^{-1})
165	12	4	164	12	4	159	15	15	$\nu_{trans}(Ca^{2+})$	−0.0079
201	12	4	201	12	4	196	20	17	ν_{trans}(AlO)	−0.0074
233	13	4	232	13	4	224	10	13	δ_{lib}(AlO)	−0.0113
266	25	5	264	25	5	250	15	20	–	−0.0201
280	2	7	278	2	7	267	5	17	–	−0.0152
347	11	8	345	11	8	331	17	21	–	−0.0199
–	–	–	350	1	20	348	7	39	–	−0.0025
395	9	8	393	8	8	382	6	23	–	−0.0172
457	3	18	453	3	18	–	–	–	–	−0.0305
477	2	6	476	2	6	469	12	27	–	−0.0095
500	8	14	498	8	14	–	–	–	$\delta(AlO_4)$	−0.0408
506	100	9	505	100	9	493	100	30	$\nu_{rot}(AlO_6)$	−0.0170
592	3	5	590	3	6	576	1	14	–	−0.0213
708	1	9	708	2	33	–	–	–	$\nu_s(AlO_6)$	−0.0061
739	23	4	738	20	5	722	21	23	$\nu_s(AlO_4)$	−0.0235
772	89	11	772	76	13	766	49	31	–	−0.0089
803	10	64	804	13	73	789	22	54	–	−0.0176

$$\Gamma_{vib} = 14A_1 + 11A_2 + 13B_1 + 15B_2 = 53. \quad (1)$$

All modes except A_2, which are only Raman-active, are both Raman- and IR-active. The experimentally derived spectrum of polycrystalline $Ca_2Al_2O_5$ at ambient temperature is displayed in Fig. 5. There are 15 bands with relative intensities ≥ 1 (integrated areas related to the most intense band at 506 cm^{-1}) that could be detected (Table 5). The three bands marked with arrows in Fig. 5 result from the underlying sapphire sample holder.

For the calcium ferrite-type $CaAl_2O_4$ (Kojitani *et al.*, 2003) crystals bands higher than *ca* 550 cm^{-1} were assigned to stretching modes of AlO_6 octahedra $\nu_s(AlO_6)$. Bands between 250 and 550 cm^{-1} were due to rotational modes of AlO_6 octahedra, $\nu_{rot}(AlO_6)$, and translational modes of Al^{3+}, $\nu_{trans}(Al^{3+})$, and bands below 250 cm^{-1} to translational modes of Ca^{2+}, $\nu_{trans}(Ca^{2+})$. Calcium ferrite-type $CaAl_2O_4$ is built up of double chains of edge-shared AlO_6 octahedra in contrast to $Ca_2Al_2O_5$ at room temperature, where layers of AlO_6 octahedra and *zweier* single chains of AlO_4 tetrahedra are the main building units (Kahlenberg *et al.*, 2000). A Raman study of $K_2Al_2B_2O_7$ (Hu *et al.*, 2004), which is formed by layers of AlO_4 tetrahedra and BO_3 triangles, reported bands between 780–1000 and 480–540 cm^{-1}, and assigned them to stretching and bending vibrations of the tetrahedron $\nu_s(AlO_4)$ and $\delta(AlO_4)$. Bands between 69 and 360 cm^{-1} were attributed by the authors to external vibrations originating from translational motions of the K ion, $\nu_{trans}(K^+)$, and $Al_2(BO_3)_2$ anion groups plus the librational motion of the anion group, $\delta_{lib}[Al_2(BO_3)_2]$.

Referring to the citations above, the two intense bands in the spectrum at 772 and 739 cm^{-1} (Fig. 5) probably reflect $\nu_s(AlO_4)$ and $\nu_s(AlO_6)$. The lower wavenumber of $\nu_s(AlO_6)$ is consistent with the larger interatomic distances within the octahedral units (Table 3). The strongest band in the spectrum at 506 cm^{-1} is more likely related to $\delta(AlO_4)$ than to $\nu_{rot}(AlO_6)$. Various chain silicates like jadeite, $NaYSi_2O_6$ (Többens *et al.*, 2005), $Na_6Si_8O_{19}$ (Krüger *et al.*, 2005) and $K_4SrSi_3O_9$ (Kahlenberg *et al.*, 2007) show very similar spectra with intense bands around 900–1100 and 450–700 cm^{-1}, related to SiO_4 tetrahedra stretching and bending vibrations. The higher wavenumber can be explained by the stronger bonding and shorter interatomic distances of Si—O compared with Al—O. The bands below 500 cm^{-1} result presumably from $\nu_{trans}(Ca^{2+})$, ν_{trans}(AlO) and δ_{lib}(AlO).

Raman experiments were also carried out at elevated temperatures starting from 373–1073 K in steps of 100 K. The results are summarized in Fig. 6. The temperature depen-

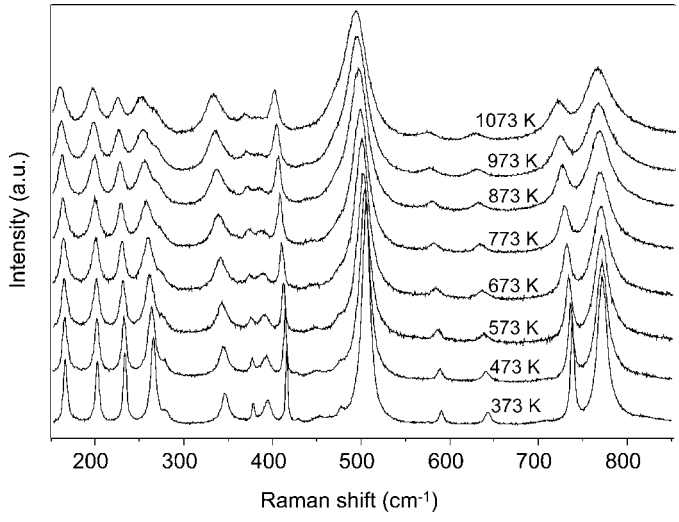

Figure 6
Raman spectra of $Ca_2Al_2O_5$ at elevated temperatures from 373 to 1073 K.

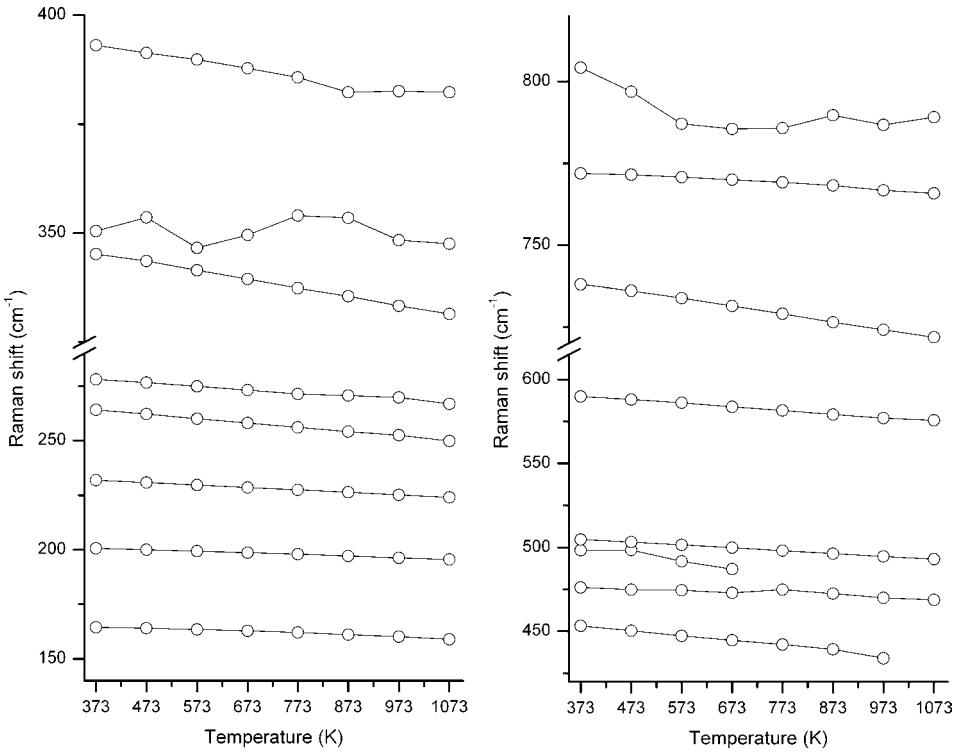

Figure 7
Temperature dependence of the positions of the observed Raman bands, as determined from eight measured spectra in the region from 373 to 1073 K.

dence, $\Delta\nu/\Delta T$, of the observed bands is displayed in Fig. 7 and Table 5. $\Delta\nu/\Delta T$ of all the vibrational modes are approximately linear and within a narrow interval, with some exceptions:

(i) $\Delta\nu/\Delta T$ of $\nu_s(AlO_4)$ is significantly lower than $\Delta\nu/\Delta$T of $\nu_s(AlO_6)$ (Table 5). Furthermore, $\Delta\nu/\Delta T$ of the $\delta(AlO_4)$ vibrational mode at 476 cm^{-1} is comparably low. This is probably related to the higher bond forces within the tetrahedron compared with the octahedron.

(ii) At first sight the only difference between the Raman spectra at 373 and 1073 K seems to be the peak broadening. However, detailed analysis of the deconvoluted spectral region between 400 and 500 cm^{-1} clearly showed the disappearance of two modes at 673 and 973 K, respectively (Fig. 7). This mode reduction may be an indication of the slight symmetry change from *I*2*mb* at room temperature to the (3 + 1)-dimensional superspace group *Imma*(00γ)*s*00. However, to the best of our knowledge, studies on the influence of structure modulations affecting vibrational spectra have not been available up to now, so this assumption remains associated with some uncertainty.

(iii) $\Delta\nu/\Delta T$ of two vibrational modes around 800 and 350 cm^{-1} clearly deviate from linearity (Fig. 7). The 350 cm^{-1} mode could not be detected at room temperature. Luminescence and/or fit uncertainties of these broad and weak bands may play a role here.

5. Conclusions

$Ca_2Al_2O_5$ is the second example of a brownmillerite structure showing an incommensurate ordering of tetrahedral chains at high temperatures. As these two examples are the end-members of the solid-solution series $Ca_2(Fe_{1-x}Al_x)_2O_5$, it can be assumed that intermediate compositions show a similar behaviour. Fukuda & Ando (2002) as well as Redhammer *et al.* (2004) have already examined the compositional dependence of the phase transition in the range $x = 0$ to $x = 0.235$ and $x = 0.325$, respectively. Towards higher aluminium contents their results differ significantly. Apart from this discrepancy, the phase boundary in the $x > 0.325$ region is still unknown. Possible reasons for the occurrence of incommensurate high-temperature phases were identified, but further studies on the phase transitions are required to reveal more details of the $Ca_2(Fe_{1-x}Al_x)_2O_5$ system, which may also be valuable for the understanding of compositionally more complex brownmillerites.

Financial support for this work has been received from the Austrian Science Fund (FWF) under the grant P17104.

References

Abakumov, A. M., Alekseeva, A. M., Rozova, M. G., Antipov, E. V., Lebedev, O. I. & Van Tendeloo, G. (2003). *J. Solid State Chem.* **174**, 319–328.
Abakumov, A. M., Kalyuzhnaya, A. S., Rozova, M. G., Antipov, E. V., Hadermann, J. & Van Tendeloo, G. (2005). *Solid State Sci.* **7**, 801–811.
Abakumov, A. M., Rozova, M. G., Pavlyuk, B. P., Lobanov, M. V., Antipov, E. V., Lebedev, O. I., Van Tendeloo, G., Ignatchik, O. L., Ovtchenkov, E. A., Koksharov, Y. A. & Vasil'ev, A. N. (2001). *J. Solid State Chem.* **160**, 353–361.
Aggarwal, P. S., Gard, J. A., Glasser, F. P. & Biggar, G. M. (1972). *Cem. Concr. Res.* **2**, 291–297.
Battle, P. D., Bell, A. M. T., Blundell, S. J., Coldea, A. I., Gallon, D. J., Pratt, F. L., Rosseinsky, M. J. & Steer, C. A. (2002). *J. Solid State Chem.* **167**, 188–195.
Berastegui, P., Eriksson, S. & Hull, S. (1999). *Mater. Res. Bull.* **34**, 303–314.
Brandenburg, K. & Berndt, M. (2001). *DIAMOND*, Version 3.1e. Crystal Impact, Bonn, Germany.
Brown, I. D. & Altermatt, D. (1985). *Acta Cryst.* B**41**, 244–247.

Colville, A. A. & Geller, S. (1971). *Acta Cryst.* B**27**, 2311–2315.
Dowty, E. (2000). *ATOMS*, Version 5.1. Shape Software, Kingsport, USA.
Dowty, E. (2006). *VIBRATZ.* Shape Software, Kingsport, USA.
Fukuda, K. & Ando, H. (2002). *J. Am. Ceram. Soc.* **85**, 1300–1303.
Greaves, C., Jacobson, A. J., Tofield, B. C. & Fender, B. E. F. (1975). *Acta Cryst.* B**31**, 641–646.
Hadermann, J., Abakumov, A. M., D'Hondt, H., Kalyuzhnaya, A. S., Rozova, M. G., Markina, M. M., Mikheev, M. G., Tristan, N., Klingeler, R., Büchner, B. & Antipov, E. V. (2007). *J. Mater. Chem.* **17**, 692–698.
Hansen, W. C., Brownmiller, L. T. & Bogue, R. H. (1928). *J. Am. Chem. Soc.* **50**, 396–406.
Horiba Jobin Yvon (2004). *LabSpec*, Version 4.14. Horiba Jobin Yvon, New Jersey, USA.
Hu, X. B., Wang, J. Y., Zhang, C. Q., Xu, X. G., Loong, C.-K. & Grimsditch, M. (2004). *Appl. Phys. Lett.* **85**, 2241–2243.
Janssen, T., Janner, A., Looijenga-Vos, A., de Wolff, P. M. & Prince, E. (2004). *International Tables for Crystallography*, Vol. C, ch. 9.8. Dordrecht: Kluwer Academic Publishers.
Kahlenberg, V., Fischer, R. & Shaw, C. S. J. (2000). *Am. Mineral.* **85**, 1061–1065.
Kahlenberg, V., Kaindl, R. & Sartory, B. (2007). *Solid State Sci.* **9**, 65–71.
Kahlenberg, V. & Shaw, C. S. J. (2001). *Z. Kristallogr.* **216**, 206–209.
Kojitani, H., Nishimura, K., Kubo, A., Sakashita, M., Aoki, K. & Akaogi, M. (2003). *Phys. Chem. Miner.* **30**, 409–415.
Krekels, T., Milat, O., Van Tendeloo, G., Amelinckx, S., Babu, T. G. N., Wright, A. J. & Greaves, C. (1993). *J. Solid State Chem.* **105**, 313–335.
Kroumova, E., Aroyo, M. I., Perez-Mato, J. M., Kirov, A., Capillas, C., Ivantchev, S. & Wondratschek, H. (2003). *Phase Transitions*, **76**, 155–170.
Krüger, H. & Kahlenberg, V. (2005). *Acta Cryst.* B**61**, 656–662.
Krüger, H., Kahlenberg, V. & Kaindl, R. (2005). *Solid State Sci.* **7**, 1390–1396.
Krüger, H., Petříček, V. & Kahlenberg, V. (2006). *Aperiodic'06 Conference Abstracts*, pp. 28–29.
Lambert, S., Heligny, H., Grebille, D., Pelloqiun, D. & Raveau, B. (2002). *Chem. Mater.* **14**, 1818–1826.
Milat, O., Krekels, T., Van Tendeloo, G. & Amelinckx, S. (1993). *J. Phys. I*, **3**, 1219–1234.
Mirwald, P. W., Getting, J. C. & Kennedy, G. C. (1975). *J. Geophys. Res.* **80**, 1519–1525.
Petříček, V., Dušek, M. & Palatinus, L. (2000). *JANA*2000. Institute of Physics, Prague, Czech Republic.
Redhammer, G. J., Tippelt, G., Roth, G. & Amthauer, G. (2004). *Am. Mineral.* **89**, 405–420.
Robinson, K., Gibbs, G. V. & Ribbe, P. H. (1971). *Science*, **171**, 567–570.
Stoe & Cie (2005). *X-Area*. Stoe & Cie GmbH, Darmstadt, Germany.
Taylor, H. F. W. (1997). *Cement Chemistry*, 2nd ed. London: Thomas Telford.
Többens, D. M., Kahlenberg, V. & Kaindl, R. (2005). *Inorg. Chem.* **44**, 9554–9560.
Wolff, P. M. de (1974). *Acta Cryst.* A**30**, 777–785.